PIER C

(Received 16 November 2025, Accepted 8 December 2025, Scheduled 3 January 2026)

Bandwidth-Enhanced Waveguide-Fed Metasurface Antennas Based on CELC Polarizability Mapping

Ivan Diaz[1, 2, *], Carlos Suarez[1], Juan Baena[3], and Hector Guarnizo[2]

[1] *Department Engineering, Universidad Distrital F.J.C., Bogotá D.C., Colombia*
[2] *Department Engineering, Universidad El Bosque, Bogota D.C., Colombia*
[3] *Department of Physics, Universidad Nacional de Colombia, Bogotá D.C., Colombia*

ABSTRACT: This work presents the design, characterization, and experimental validation of waveguide-fed metasurface antennas based on complementary electric-LC (CELC) resonators. The magnetic polarizability of individual unit cells was extracted using the Incremental Difference Method, enabling physically grounded complex weighting of each metasurface element without the need for external feeding networks. Two CELC geometries (square and circular) were investigated under identical WR340 waveguide excitation. The circular CELC exhibited a smoother current distribution and a more uniform polarizability profile, as observed in the polarizability-mapping results, whereas the square CELC provided a slightly higher gain owing to its sharper magnetic resonance. Lateral-slot perturbations were introduced as a simple geometric modification to overcome the intrinsic narrowband nature of Lorentz-type resonators. The simulated and measured results confirm a significant improvement in impedance bandwidth, reaching 194 MHz (simulated) and 189 MHz (measured) for the square slot geometry, and 222 MHz (simulated) and 209 MHz (measured) for the circular slot geometry. Radiation-pattern measurements in an indoor antenna chamber showed good agreement with full-wave simulations, validating the polarizability-based weighting mechanism and the overall metasurface antenna model. The results demonstrate that magnetic-polarizability mapping combined with geometry-tailored perturbations provides an effective and experimentally verified approach for compact and bandwidth-enhanced metasurface antenna design.

1. INTRODUCTION

Metamaterials and metasurfaces enable the subwavelength control of electromagnetic waves, providing tailored amplitude, phase, and polarization responses across microwaves to optical bands [1–3]. In particular, metasurface antennas offer low-profile and efficient beamforming capabilities by using engineered unit cells to shape aperture fields [4, 5].

Programmable and reconfigurable metasurfaces have been proposed for beyond-5G and 6G systems [6–10], although most implementations rely on planar apertures and distributed feed, with several wideband and reconfigurable metasurface antenna realizations reported in the literature [11–13]. Waveguide-fed metasurface antennas overcome these limitations by leveraging the robustness and high-power handling of metallic waveguides while using subwavelength resonant elements to couple the guided mode to free space [14–16]. However, their performance, however, is strongly constrained by the Lorentzian dispersion of the unit cells and the narrow impedance-matching region characteristic of resonant inclusions.

CELC-type resonators were used as magnetic metamaterial elements [17–19, 21, 22]. Although analytical polarizability models and GSTC-based formulations exist [20, 23], practical design requires reliable extraction of polarizability under realistic excitation. In a prior work, the authors introduced an Incremental Difference Method to estimate the magnetic polarizability of square CELC cells embedded in a WR340 waveguide and numerically demonstrated metasurface beam synthesis [24]. However, that study did not include experimental validation nor consider bandwidth-enhanced geometries.

Because resonant inclusions inherently trade phase coverage for usable amplitudes, their Lorentzian behavior limits the effective bandwidth and robustness of passive metasurface antennas [14, 16]. Standard CELC designs further exhibit narrow matching regions and sensitivity to fabrication tolerances, motivating experimentally validated approaches that can confirm polarizability extraction and incorporate geometry-level bandwidth improvement.

This work experimentally validates CELC-based waveguide-fed metasurface antennas and introduces bandwidth-enhanced unit cell designs. Square and circular CELC apertures were fabricated and characterized through measured reflection coefficients, and lateral-slot perturbations were investigated as a means to broaden the operational bandwidth while preserving magnetic resonance. The Incremental Difference Method was applied to interpret the measured responses in terms of the effective magnetic polarizability.

The main contributions of this study are summarized as follows: First, to the best of our knowledge, we provide the first experimental validation of the Incremental Difference Method for extracting the magnetic polarizability of CELC unit cells under realistic waveguide-fed excitation. Second, we performed a direct comparison between square and circular CELC geome-

* Corresponding author: Ivan Diaz (iediaz@unbosque.edu.co).

tries implemented on the same WR340 platform, quantifying how symmetry and the effective quality factor influence polarizability mapping and the resulting metasurface weighting. Third, we introduce and experimentally verify a bandwidth-enhancement strategy based on lateral slot perturbations, which is fully compatible with polarizability-based design, leading to improved $|S_{11}|$ performance without additional feed-network complexity.

2. THEORETICAL BACKGROUND

Metasurface antennas composed of subwavelength resonant inclusions can be modeled using their effective electric and magnetic polarizabilities, which describe the induced dipole moments under external electromagnetic excitation [11–13]. For a unit cell embedded in a guided-wave environment, the instantaneous dipole moments can be expressed as

$$\mathbf{p} = \varepsilon_0 \alpha_e \mathbf{E}_{\text{local}}, \tag{1}$$

$$\mathbf{m} = \alpha_m \mathbf{H}_{\text{local}}, \tag{2}$$

where α_e and α_m denote the electric and magnetic intrinsic polarizabilities, respectively, and $\mathbf{E}_{\text{local}}$ and $\mathbf{H}_{\text{local}}$ represent the local fields, including mutual interactions [1, 20]. CELC resonators are primarily magnetic inclusions whose response is dominated by α_m, following the same physical principles governing other complementary resonators such as CSRRs and related structures [19, 21, 22].

Near resonance, the magnetic polarizability of a CELC inclusion is described well by a Lorentz-type analytical function [17, 18]:

$$\alpha_m(\omega) = \frac{F\omega^2}{\omega_0^2 - \omega^2 + j\Gamma\omega}, \tag{3}$$

where F is the oscillator strength, ω_0 the resonance frequency, and Γ the damping factor, which account for conduction loss, radiation leakage, and material dissipation. Equation (3) predicts two key features: (i) the real part of α_m crosses zero at $\omega = \omega_0$ and governs amplitude shaping and (ii) the imaginary part reaches its maximum at resonance, determining the available phase range. Monotonic phase variation across the resonance is intrinsic to the resonant elements and limits the achievable phase coverage when used for beam steering or holographic modulation [14, 16].

For a short-circuited waveguide operating in the dominant TE_{10} mode, the excitation establishes a standing-wave pattern along the longitudinal z-axis. The local magnetic field at position z_i of the i-th inclusion can be approximated as

$$H_{\text{local}}(z_i) \propto \sin(\beta_{10} z_i), \tag{4}$$

where β_{10} is the propagation constant of the TE_{10} mode.

$$m_i(\omega) = \alpha_{m,i}(\omega) \mathbf{H}_{\text{local}}(z_i), \tag{5}$$

which directly modulates the radiation contribution. For an array of N inclusions, the resulting radiation diagram is approximated by

$$AF(\phi) = \sum_{i=1}^{N} \alpha_{m,i}(\omega) e^{j(-\beta z_i + k z_i \sin\phi)}, \tag{6}$$

where β is the propagation constant of the TE_{10} mode. Equation (6) indicates that the amplitude and phase of the polarizability dictate the weighting coefficients of the metasurface antenna. Amplitude weighting is constrained by $|\alpha_m|$, and phase control is limited by the Lorentzian phase swing inherent to Equation (3).

In practical implementations, the polarizability of a unit cell can be inferred from the perturbation of its reflection coefficient. For a waveguide excited from a single port, the incremental difference

$$\Delta S_{11}(\omega) = S_{11,\text{with cell}}(z_i) - S_{11,\text{empty}}, \tag{7}$$

captures the local scattering introduced by resonator at position z_i. Under small-perturbation assumptions, the magnitude and phase of ΔS_{11} are proportional to those of the induced magnetic dipole moment, and therefore to the polarizability [22, 23]:

$$\alpha_m(\omega) \propto \frac{\Delta S_{11}(\omega)}{\mathbf{H}_{\text{local}}}. \tag{8}$$

This relationship was numerically validated in prior work [24]. The Lorentzian nature of Equation (3) limits the operational bandwidth and achievable phase range of CELC-based metasurfaces [14, 16]. In this context, geometric modifications, such as introducing lateral slots, can alter the effective inductance and capacitance of the resonator, adjust ω_0 and reduce Γ, thereby broadening the useful frequency region while maintaining the required phase gradient for metasurface radiation.

3. DESIGN OF CELC-BASED RADIATING CELLS

CELC inclusions are widely used as magnetic resonators for metasurface antennas owing to their subwavelength size, strong magnetic response, and ease of fabrication in metallic waveguide platforms [21, 22]. In this study, two CELC geometries were investigated: a conventional square CELC and a circular CELC. Both structures were implemented as complementary apertures on the broad wall of a WR340 waveguide, enabling direct coupling to the TE_{10} magnetic field. The subsequent sections introduce the simple slot perturbations applied to each geometry to enhance the operational bandwidth.

3.1. Square CELC Geometry

The square CELC unit cell used in this work is based on the well-known Electric-LC (ELC) resonator originally introduced by Schurig, Mock, and Smith in [21]. The structure employed here corresponds to its complementary version (CELC), in which the metallic and void regions of the canonical ELC are inverted according to Babinet's principle. As shown in Figure 1, the white region represents the etched aperture on the metallic surface, whereas the surrounding gray region corresponds to the conducting plate.

The square CELC consists of a complementary electric LC aperture formed by two horizontal gaps and two vertical conducting paths that define a closed current loop in its dual (complementary) form. Magnetic resonance arises from the circulating surface currents induced around the aperture and the

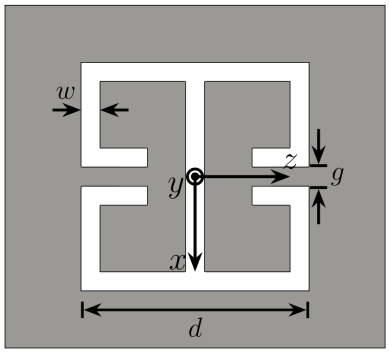

FIGURE 1. Square CELC unit cell derived from the complementary Electric-LC resonator introduced in [21]. The white region denotes the etched aperture on the metallic surface. The nominal geometric parameters are $w = 2\,\text{mm}$ (arm thickness), $g = 2\,\text{mm}$ (bridge width), and $d = 18\,\text{mm}$ (outer cell width). During operation, the parameter d is varied to tune the magnetic polarizability α_m required for the metasurface weighting.

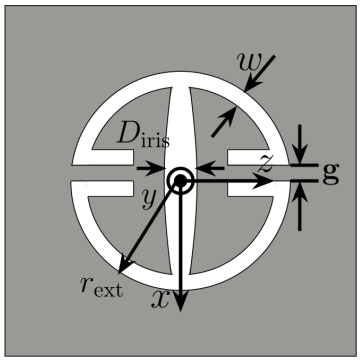

FIGURE 2. Circular CELC unit cell inspired by the efficient complementary resonator proposed in [25]. The aperture is defined by the external radius r_{ext}, the iris width $D_{\text{iris}} = 4\,\text{mm}$, the arm thickness $w = 2\,\text{mm}$, and the bridge width $g = 2\,\text{mm}$. The nominal radius is $r_{\text{ext}} = 11\,\text{mm}$, which is varied during operation to tune the magnetic polarizability α_m. Owing to its rotational symmetry, the circular CELC exhibits smoother current distribution and reduced sensitivity to angular misalignment compared with the square geometry.

electric-field concentration across the horizontal gaps. The main geometrical parameters are (i) d, the outer width of the square aperture; (ii) w, the arm thickness; and (iii) g, the width of the horizontal gaps, which provides the capacitive loading of the resonator.

These parameters jointly determine the effective inductive and capacitive loading of the complementary resonator, and therefore, its magnetic polarizability and resonance frequency. Owing to its dominant magnetic response and well-confined LC-type behavior, a square CELC is employed in this work as the fundamental radiating element for controlling the phase and amplitude weights that shape the antenna radiation pattern. This geometry provides clear and predictable Lorentz-type polarizability, making it an appropriate baseline for implementing and validating the Incremental Difference Method under waveguide-fed excitation.

3.2. Circular CELC Geometry

The second unit-cell geometry examined in this work is the circular CELC resonator, inspired by the efficient radiating element introduced by Yoo et al. in [25]. Their work demonstrated that circular and tapered CELC apertures exhibit improved radiation efficiency, reduced ohmic losses, and broader operational bandwidth than traditional square ELC-based inclusions, particularly in waveguide-fed metasurface configurations.

We show that a circular CELC is implemented as a complementary version of the aperture resonator, obtained by etching a circular split ring from the metallic surface, while the surrounding region remains conductive. As illustrated in Figure 2, the geometry consists of a circular void region with diameter r_{ext}, gap width c, diameter iris D_{iris}, and bridge width g. This topology yields a more uniform current distribution around the aperture and smoother magnetic field coupling than polygonal resonators.

When being embedded in the WR340 waveguide, the circular CELC preserves the dominant magnetic response characteristic of ELC-type inclusions while exhibiting reduced sensitivity to fabrication tolerances and a slightly lower quality factor. Consequently, the resonant behavior appears less abrupt, and the reflection coefficient $|S_{11}|$ tends to present a broader minimum. These properties make the circular CELC a practical alternative for metasurface antennas, in which maintaining a predictable Lorentz-type phase response is necessary, but a modest increase in operational bandwidth is desired. Moreover, its rotational symmetry eliminates the orientation-dependent variations observed in the square CELC apertures, making the magnetic coupling to the TE_{10} standing-wave field more uniform and less sensitive to small rotational misalignments during fabrication or assembly.

3.3. Bandwidth-Enhanced CELC with Lateral Slots

Once the metasurface array is synthesized using magneticpolarizability mapping to guarantee broadside radiation, lateral slots are incorporated as an additional geometric perturbation to enhance the impedance bandwidth of the antenna. These slots operate in a manner analogous to classical slotted-waveguide antennas; they couple directly to the TE_{10} standing-wave field, introduce an auxiliary radiation mechanism, and redistribute the stored energy around the main CELC resonance. As a result, the impedance variation near resonance becomes smoother, and the antenna remains matched over a wider frequency range without altering the phase profile imposed by the CELC array.

A key design consideration is that the slots are positioned to minimize their interaction with the local magnetic fields that drive the CELC apertures. This ensures that the magnetic polarizability of each resonator is only weakly perturbed, preserving the broadside beam predicted by polarizability-based weighting while still providing a measurable increase in the $|S_{11}|$ bandwidth. The slot-enhanced designs remain fully compatible with the Incremental Difference Method, enabling direct experimental extraction of their effective magnetic polarizability and comparison with unmodified geometries.

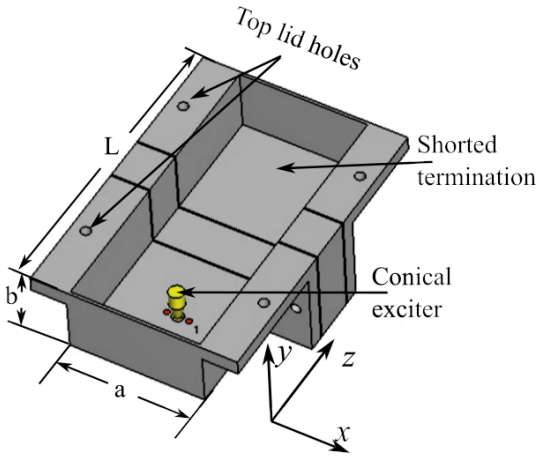

FIGURE 3. WR340 waveguide section used as the cavity for the metasurface antenna prototype. The internal dimensions correspond to $a = 86.36\,\text{mm}$ and $b = 43.18\,\text{mm}$, and the short-circuited cavity region has a length $L = 198.31\,\text{mm}$. A coaxial probe provides excitation of the TE_{10} mode, while the upper metallic surface includes alignment holes for mounting the interchangeable metasurface plates. This cavity length supports a strong longitudinal standing-wave pattern, enabling the spatially dependent magnetic excitation required for the Incremental Difference Method.

4. ANTENNA MODEL AND MAGNETIC POLARIZABILITY MAPPING

4.1. Waveguide-Fed Antenna Base Structure

The metasurface antenna was implemented using a WR340 waveguide section, excited by a coaxial probe operating in the dominant TE_{10} mode. The shorted termination reflects the guided wave and generates a longitudinal standing-wave pattern whose spatial variation in the magnetic-field amplitude is essential for applying the Incremental Difference Method.

Figure 3 shows the metallic cavity used as the antenna base. It includes the coaxial-probe transition and the upper mounting plane for interchangeable CELC plates. The cavity dimensions follow the standard WR340 specifications, and the global coordinate system adopts z as the longitudinal axis of the waveguide, x is the transverse dimension, and y is the outward normal (broadside radiation direction).

4.2. Linear CELC Array on the Upper Plate

A removable metallic plate containing a linear array of six CELC resonators is mounted on the short-circuited section of the WR340 cavity of length $L = 198.31\,\text{mm}$, corresponding to approximately $1.34\lambda_g$ at 2.45 GHz. This aperture length provides sufficient longitudinal variation of the standing-wave magnetic field required for the Incremental Difference Method, while keeping all elements within the subwavelength regime.

The number of resonators and their spacing follow the metasurface-antenna guidelines in [14], where the proper aperture sampling is satisfied for $\lambda_0/10 < d < \lambda_0/5$. At 2.45 GHz, this interval accommodates six CELCs without approaching the $\lambda_0/2$ spacing typical for phased arrays. Because CELC elements cannot impose arbitrary phase shifts, maintaining subwavelength spacing ensures that complex weights arise from the magnetic polarizability rather than from the feed network.

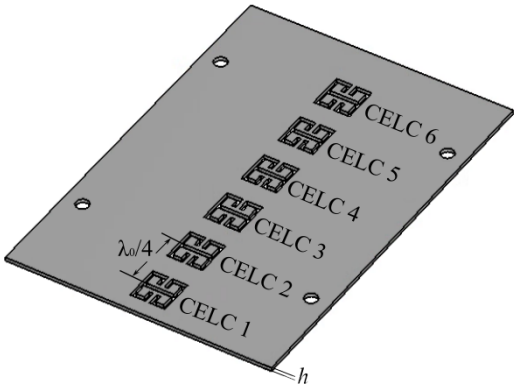

FIGURE 4. Upper metallic plate containing a linear array of six square CELC apertures mounted on the WR340 waveguide. The longitudinal placement of each resonator samples a different point of the standing-wave magnetic field, enabling the extraction of the spatially dependent magnetic polarizability $\alpha_{m,i}$.

Each CELC was placed at a distinct longitudinal position along the z-axis, sampling different points of the TE_{10} standing wave created by the shorted termination. Unlike a normally terminated waveguide with a nearly uniform traveling-wave amplitude, the cavity exhibits a sinusoidally varying magnetic field; therefore, each resonator experiences a different local excitation $\mathbf{H}_{\text{loc}}(z_i)$ and yields a distinct extracted polarizability.

Figure 4 shows an array of six square CELC apertures. The resulting spatial variation of the extracted $\alpha_{m,i}$ is directly linked to the radiation characteristics of the metasurface: elements near the magnetic-field maxima exhibit stronger coupling, whereas those near the minima contribute weakly. This spatially dependent weighting forms the basis of the polarizability-driven radiation model developed in the following section.

4.3. Incremental Difference Mapping of Square CELC Resonators

The Incremental Difference Method was applied to the six-cell array to quantify the magnetic response of each resonator from the perturbation introduced in the reflection coefficient. By comparing the S_{11} variation produced when a single aperture was modified, the effective magnetic polarizability $\alpha_{m,i}$ was extracted directly.

The proportionality $\Delta S_{11} \propto \alpha_m H_{\text{loc}}$ follows from the classical small-perturbation theory for resonant cavities (Collin, Pozar), in which each CELC aperture perturbs the boundary locally without altering the global mode structure. In this linear regime, the incremental reflection response is directly related to the induced magnetic dipole moment and, therefore, to the magnetic polarizability. This behavior was validated in our earlier PIER C publication [24], where full-wave simulations demonstrated a clear linear correlation between H_{loc} and ΔS_{11}. Fabrication tolerances of ± 0.1–$0.2\,\text{mm}$ produce shifts of only 2–4% in the extracted α_m, consistent with the small frequency deviations observed experimentally, confirming the robustness of the method.

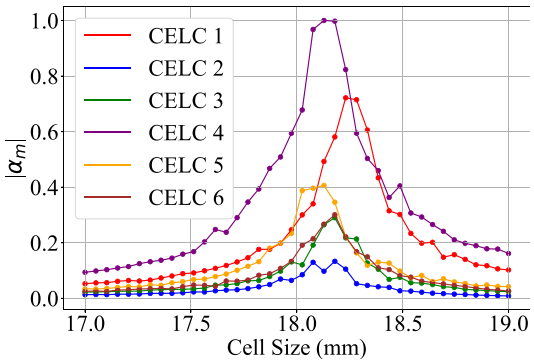

FIGURE 5. Normalized magnitude of the extracted magnetic polarizability $|\alpha_m|$ for the six square CELC resonators as a function of the external width d. The different peak amplitudes reflect the spatial variation of the standing magnetic field inside the WR340 waveguide.

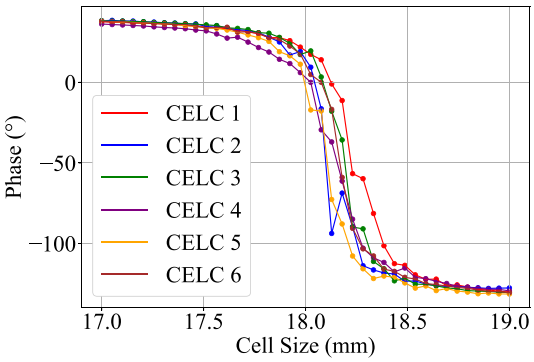

FIGURE 6. Phase of the extracted magnetic polarizability $\angle\alpha_m$ for the six square CELC resonators as a function of the external width d. Sharper transitions occur at positions with stronger magnetic coupling.

For square CELC geometry, the term *cell size* refers explicitly to the external width d of the aperture (see Figure 1). By sweeping d around its nominal resonant value while keeping the remaining parameters fixed, the characteristic Lorentz-type magnitude and phase profiles of α_m were obtained at the six array positions.

Figure 5 shows the normalized magnitude of the extracted polarizability as a function of d. Although all resonators peak near their respective resonance, the amplitude varies across the array due to the standing-wave distribution inside the waveguide: apertures located near magnetic-field maxima (e.g., CELC 4) exhibit stronger coupling and larger $|\alpha_m|$, whereas those near minima contribute only weakly.

The corresponding phase evolution in Figure 6 exhibits the expected Lorentzian transition from approximately $+25°$ to $-130°$. Elements with stronger magnetic coupling showed steeper phase slopes, contributing more strongly to the effective aperture weighting.

Overall, the extracted $\alpha_{m,i}$ profiles mirror the standing-wave magnetic field inside the cavity. Resonators located near the magnetic-field maxima dominate the radiation process, establishing the nonuniform amplitude and phase weights that underpin the metasurface antenna operation.

4.4. Mapping of Circular CELC Resonators

A second metasurface plate containing six circular CELC apertures is mounted on the WR340 cavity with the elements located at the same axial positions as the square array, as shown in Figure 7. This ensures that both geometries sample the same standing-wave excitation, thereby enabling a direct comparison of their extracted magnetic polarizabilities.

For the circular CELC geometry, the term *cell size* refers to the external radius r_{ext} of the aperture (see Figure 2). As in the square case, the Incremental Difference Method is applied by sweeping r_{ext} around its nominal resonant value. The resulting magnitude of α_m, as shown in Figure 8, exhibits smoother variations and more uniform peak amplitudes across the array positions. This behavior follows from the rotational symmetry of the circular CELC, which promotes more homogeneous

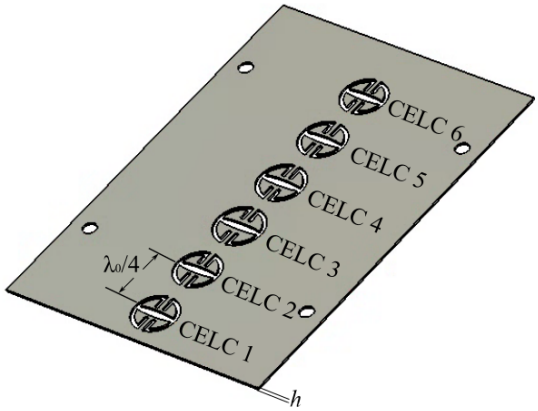

FIGURE 7. Upper metallic plate containing a linear array of six circular CELC resonators, positioned at the same axial locations as the square-CELC configuration for direct comparison of the magnetic polarizability mapping.

current distributions and reduces the sensitivity to small misalignments.

The corresponding phase response in Figure 9 retains the Lorentzian transition with generally less abrupt slopes than the square geometry. This indicates a lower effective quality factor and broader usable bandwidth while preserving the phase behavior required for metasurface beam control. The reduced variability among the elements reflects a more uniform magnetic coupling along the waveguide.

Overall, the circular CELC provided a more homogeneous magnetic response across the array, with broader magnitude peaks and smoother phase transitions. This uniformity facilitates metasurface aperture design and improves the tolerance to fabrication variations while maintaining a dominant magnetic resonance compatible with the Incremental Difference Method.

5. ANTENNA DESIGN BASED ON POLARIZABILITY MAPPING

The magnetic polarizability mapping obtained in the previous section provides direct insight into the radiating strength of each CELC element and enables informed design of the metasurface

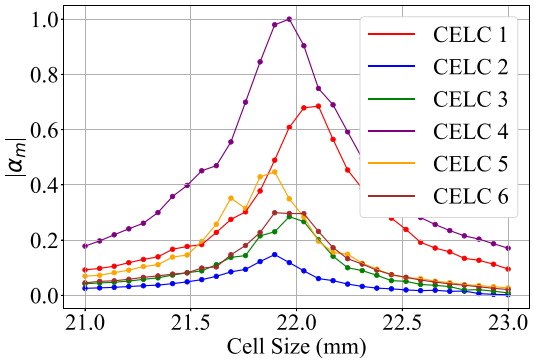

FIGURE 8. Normalized magnitude of the extracted magnetic polarizability $|\alpha_m|$ for the circular CELC resonators as a function of the external radius r_{ext}. The circular geometry yields smoother variations and more uniform peak amplitudes across the array positions.

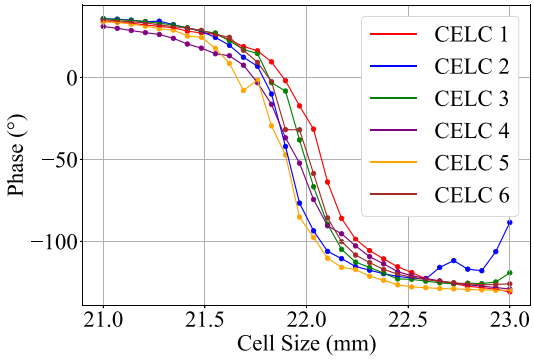

FIGURE 9. Phase of the extracted magnetic polarizability $\angle\alpha_m$ for the circular CELC resonators as a function of the external radius r_{ext}. The aperture symmetry results in smoother and more uniform phase transitions than in the square geometry.

antenna. As each resonator experiences a different local magnetic field inside the WR340 waveguide, its extracted polarizability $\alpha_{m,i}$ naturally determines its effective radiation weight. This makes the Incremental Difference Method an efficient alternative to full-wave array optimization because it provides the amplitude and phase contributions of each element without requiring iterative electromagnetic simulations.

5.1. Weighting of Array Elements

For broadside operation, the antenna is designed such that the collective phase of the magnetic polarizability values satisfies the constructive-interference condition in the direction normal to the metasurface plate, which corresponds to the global y-axis in Figure 3. The measured and simulated phase responses in Figure 6 and Figure 9 exhibit the expected Lorentzian trend, ensuring a monotonic phase evolution around the resonance and providing correct phasing for radiation along the $+y$ direction.

The magnitude response shown in Figure 5 and Figure 8 reveals that elements located near the magnetic-field maxima (e.g., positions 3 and 4) contribute significantly more to the radiation pattern than those near minima. Consequently, the array does not require externally imposed excitation weights and the spatially varying magnetic polarizability $\alpha_{m,i}(\omega)$ obtained from incremental mapping, which naturally provides both the amplitude and phase assigned to each resonator. In this sense, $\alpha_{m,i}(\omega)$ acts as the complex weighting factor in Equation (6) and is fully determined by the standing-wave magnetic field and intrinsic Lorentzian response of each CELC element. This physically derived weighting enables the metasurface antenna to form the expected broadside beam without the need for matching networks or active feed architectures.

5.2. Simulation of the Resulting Radiation Patterns

The magnetic polarizability profiles extracted for both the square and circular CELC arrays provide the complex weights required for predicting the radiation behavior of the metasurface antenna. Using the array-factor formulation in Equation (6) and weighting each element according to its corresponding $\alpha_{m,i}(\omega)$, the full-wave simulations can be directly compared with the theoretical distributions. This procedure captures both the local-field variations produced by the TE_{10} standing-wave and intrinsic Lorentzian response of each resonator.

5.2.1. Square CELC Array

Figure 10 shows the simulated radiation pattern for a six-element metasurface composed of square CELC resonators. The antenna exhibited a well-defined broadside lobe, which is consistent with the symmetric phase distribution extracted for this geometry. As expected from the mapping results in Figure 5 and Figure 6, CELC 4 dominates the radiation owing to its significantly larger polarizability magnitude.

Table 1 summarizes the normalized amplitudes and phases assigned to each resonator. These values correspond to the magnetic polarizabilities obtained at the design frequency used for broadside radiation.

TABLE 1. Extracted magnetic-polarizability weights for the square CELC array at 2.45 GHz. "Size" corresponds to the external dimension d of the CELC aperture.

Cell	Size (mm)	Amplitude (norm.)	Phase (°)
CELC1	19.0	0.1020	−130.05
CELC2	18.5	0.0270	−123.39
CELC3	19.0	0.0239	−130.49
CELC4	18.1	0.9677	−29.43
CELC5	18.2	0.3459	−87.88
CELC6	18.6	0.0619	−124.86

The strong dominance of CELC 4 and the reduced contribution from CELC 2 and CELC 3 match the expected behavior of the magnetic-field distribution inside the waveguide. The square geometry produces a sharper Lorentzian resonance and therefore a more uneven weighting across the aperture.

5.2.2. Circular CELC Array

The simulated radiation pattern for the circular CELC array is shown in Figure 11. The main lobe also appears at the broadside; however, the amplitude distribution is noticeably

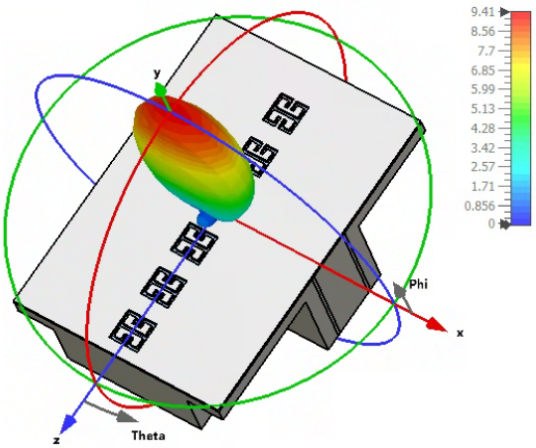

FIGURE 10. Full-wave simulated radiation pattern of the six-element square CELC metasurface antenna at 2.45 GHz. The broadside response arises from the nonuniform complex weights determined by the extracted magnetic polarizabilities.

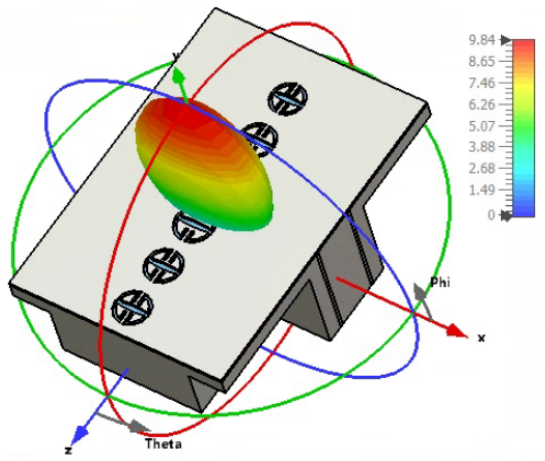

FIGURE 11. Full-wave simulated radiation pattern of the circular CELC metasurface antenna at 2.45 GHz. The circular geometry produces a smoother aperture excitation, leading to a more uniform broadside radiation pattern compared with the square case.

smoother owing to the more uniform polarizability profile of the circular geometry. This agrees with the magnitude and phase mappings observed in Figure 8 and Figure 9.

Table 2 lists the normalized amplitudes and phases used in computing the radiation pattern. The circular geometry exhibits one high-amplitude resonator (CELC 1) but overall maintains a flatter weighting profile than the square CELC configuration.

TABLE 2. Extracted magnetic-polarizability weights for the circular CELC array at 2.45 GHz. "Size" corresponds to the outer diameter $2r_{\text{ext}}$ of the circular aperture.

Cell	Size (mm)	Amplitude (norm.)	Phase (°)
CELC1	22.0	0.6081	−17.34
CELC2	22.2	0.0533	−110.54
CELC3	24.0	0.0089	−119.18
CELC4	23.0	0.1708	−129.08
CELC5	22.6	0.0606	−128.26
CELC6	21.0	0.0453	35.21

These results indicate that the circular CELC tends to produce a smoother and more uniform magnetic polarizability profile across the aperture, which leads to a less uneven excitation than the square geometry. This smoother distribution is not unique, beause different combinations of resonator sizes can produce alternative weighting profiles for a given pointing direction. However, the circular topology generally shows reduced sensitivity to dimensional variations and a slightly lower effective quality factor, traits that become more evident once the bandwidth is evaluated through the simulated and measured $|S_{11}|$ responses presented in the next section.

It is important to note that the weighting distributions listed in Tables 1 and 2 are not unique solutions. Because the magnetic polarizability of each CELC follows Lorentzian dispersion, the achievable complex weights lie on a restricted amplitude-phase manifold determined by the resonant response. Consequently, different geometric dimensions may yield nearly identical values of $\alpha_{m,i}$, leading to multiple valid configurations that produce the same radiation weighting. Therefore, polarizability mapping provides the designer with an admissible range of dimensions for each cell from which alternative solutions can be selected depending on the desired amplitude taper, fabrication constraints, or robustness requirements.

6. BANDWIDTH ENHANCEMENT VIA LATERAL SLOT PERTURBATIONS

The Lorentz-type responses of both square and circular CELC resonators inherently limit their operational bandwidths. This restriction arises from the strong confinement of currents around the aperture and the narrow capacitive gap that dominates LC resonance. To mitigate this limitation and obtain metasurface elements with an improved $|S_{11}|$ response over frequency, lateral slot perturbations were introduced into both geometries. Bandwidth improvement arises because the lateral slots redistribute the surface currents and introduce an additional capacitive-inductive path that reduces the stored reactive energy around the resonance. This lowers the effective quality factor Q, softens the impedance variation with frequency, and broadens the $|S_{11}|$ matching region, while preserving the magnetic nature of the CELC resonance.

As in classical slotted-waveguide antennas, lateral slots couple primarily to the tangential electric field on the top plate and act as a secondary radiation mechanism. This additional radiating path redistributes the stored energy around the resonance and broadens the impedance response while interacting only weakly with the magnetic polarizability of the CELC apertures.

These slots modify the effective inductive and capacitive loading of the resonators, reducing the quality factor and broadening the matching region, while preserving the magnetic nature of the resonance.

6.1. Square CELC with Lateral Slots

Figure 12 illustrates the modified square CELC geometry, in which two symmetric lateral apertures are introduced next to

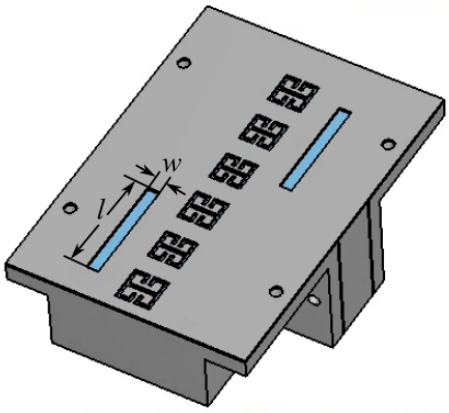

FIGURE 12. Square CELC unit cell with lateral slots introduced to reduce the effective quality factor and increase bandwidth. The perturbations modify the magnetic flux distribution and smooth the impedance transition near resonance.

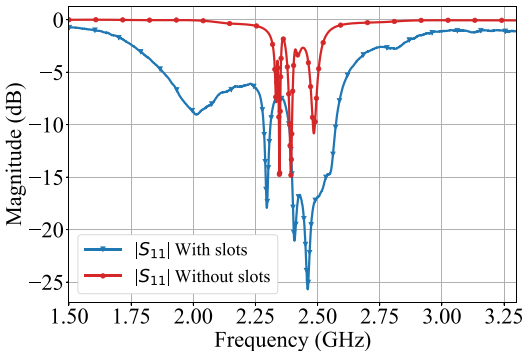

FIGURE 13. Simulated reflection coefficient $|S_{11}|$ for the square CELC with and without lateral slots. The unmodified geometry (red) exhibits a narrow high-Q resonance, while the slot-modified version (blue) shows a substantially broader impedance-matching region. The slot-modified structure achieves a 194 MHz bandwidth at the -10 dB level.

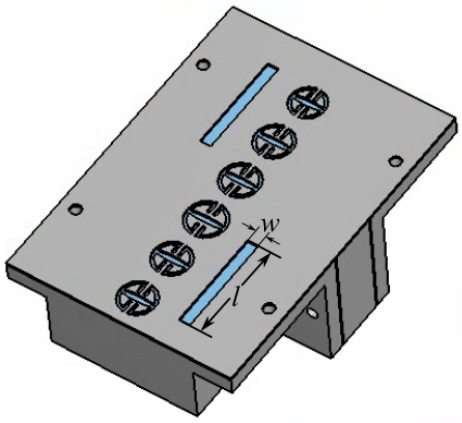

FIGURE 14. Circular CELC with lateral slot perturbations. The rotational symmetry ensures a smooth redistribution of currents and a broader resonance compared with the unmodified circular geometry.

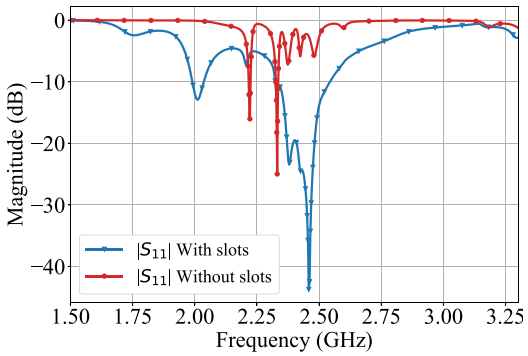

FIGURE 15. Simulated reflection coefficient $|S_{11}|$ for the circular CELC with and without lateral slots. The slot-modified geometry (blue) provides the broadest impedance-matching region among all configurations, achieving a 222 MHz bandwidth at the -10 dB level.

the main resonant structure. These perturbations alter the current paths around the aperture and increase the effective capacitive load of the resonator. The net effect is a reduction in the quality factor of the LC resonance, which leads to a smoother impedance transition and broader matching bandwidth.

The simulated reflection coefficients for the square CELC with and without slots are shown in Figure 13. The unmodified resonator (red curve) exhibited a narrow and deep resonance characteristic of a high-Q Lorentzian response. In contrast, the slot-modified version (black curve) showed a significantly wider $|S_{11}|$ dip, extending over a substantially broader frequency range while maintaining a comparable minimum reflection level. This confirms that lateral-slot perturbation effectively broadens the operational bandwidth while preserving the magnetic nature of the resonance.

6.2. Circular CELC with Lateral Slots

The same perturbation strategy is applied to the circular CELC geometry, as shown in Figure 14. Owing to the rotational symmetry of the circular aperture, the addition of lateral slots produces a more uniform redistribution of surface currents and a smoother modification of the LC resonance.

Figure 15 shows a comparison of the simulated $|S_{11}|$ response of the circular CELC with and without slots. Similar to the square geometry, the unmodified circular CELC (red curve) exhibited a sharp, narrow resonance. The slot-modified version (blue curve), however, presents the widest bandwidth among all the geometries considered, with a deep and extended matching region that spans nearly the entire band of interest. This improvement highlights the effectiveness of combining the rotational symmetry with capacitive slot perturbations to achieve enhanced bandwidth performance in metasurface antenna elements.

The slot-modified square and circular CELC resonators demonstrate that simple geometric perturbations can significantly expand the operational bandwidth while maintaining the magnetic nature of the resonance. These enhanced elements retain compatibility with the Incremental Difference Method and can be integrated into waveguide-fed metasurface antennas without altering the underlying design methodology. The next section validates the findings.

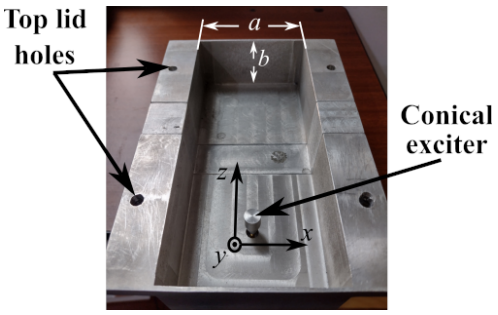

FIGURE 16. Fabricated WR340 cavity including the conical probe exciter and the mounting interface for interchangeable metasurface plates. The structure was machined to match the simulation model used for the metasurface antenna.

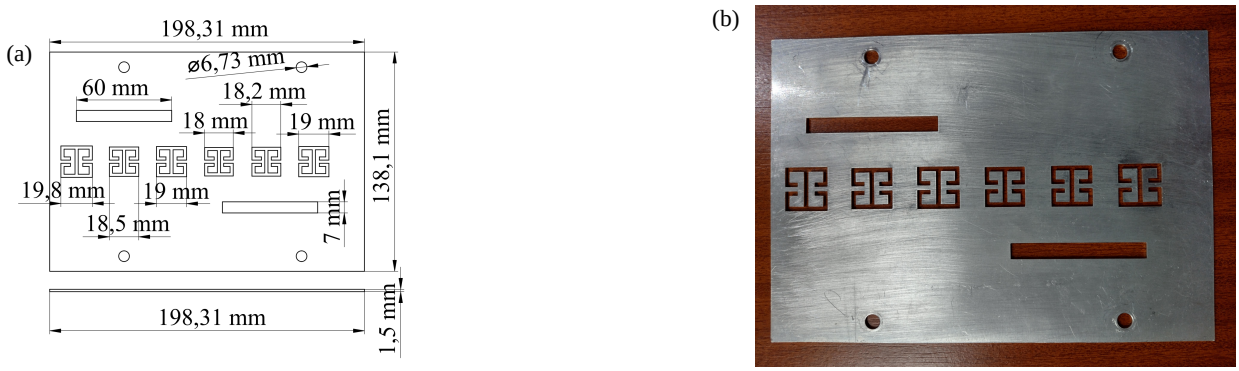

FIGURE 17. Square CELC metasurface plate with lateral slots. (a) Design drawing of the top plate. (b) Fabricated structure cut by laser in 1.5 mm aluminum (AI100, 95% purity).

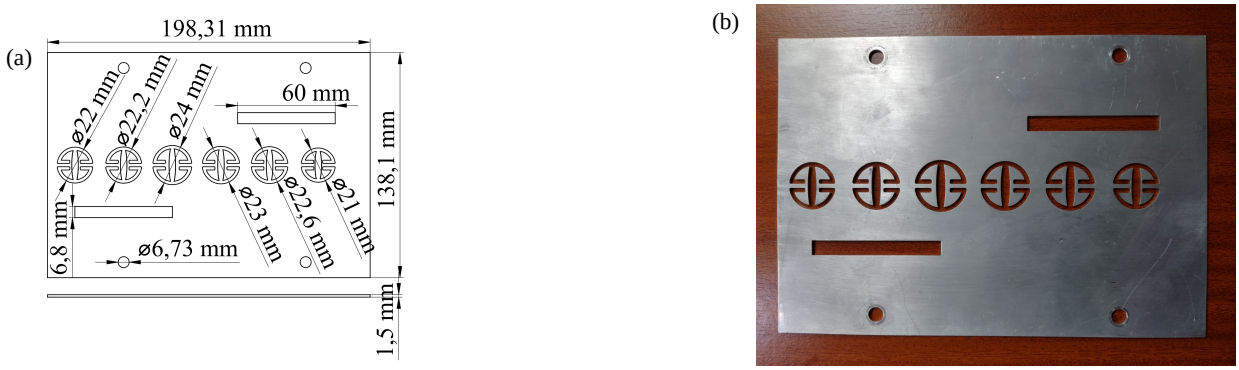

FIGURE 18. Circular CELC metasurface plate with lateral slots. (a) Design drawing of the top plate. (b) Fabricated structure cut by laser in 1.5 mm aluminum (AI100, 95% purity).

7. EXPERIMENTAL VALIDATION

To validate the metasurface antenna concept and confirm the bandwidth enhancement introduced by lateral slot perturbations, a WR340-based prototype was fabricated and experimentally characterized. All metasurface plates were manufactured using laser-cutting technology on 1.5 mm aluminum sheets (AI100, 95% purity). The fabricated structures reproduce the geometrical features of simulated CELC resonators with good dimensional accuracy, although slight edge roughness and overcut effects are unavoidable in thin aluminum laser processing.

All measurements were performed using an Anritsu S362E vector network analyzer (VNA) calibrated using a standard short-open-load-through (SOLT) procedure at the coaxial input of the waveguide.

For comparison with the measured data, full-wave simulations of the complete waveguide aperture structure were performed using the commercial solver CST Microwave Studio. These simulations model the 3D electromagnetic behavior of the cavity and metasurface plates and are entirely independent of the Incremental Difference Method, which is used solely for extracting magnetic polarizability.

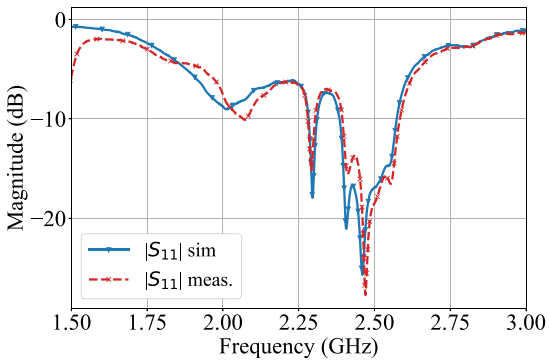

FIGURE 19. Simulated and measured reflection coefficients $|S_{11}|$ for the slot-modified square CELC metasurface. Measurement confirms the predicted bandwidth enhancement introduced by the lateral slots.

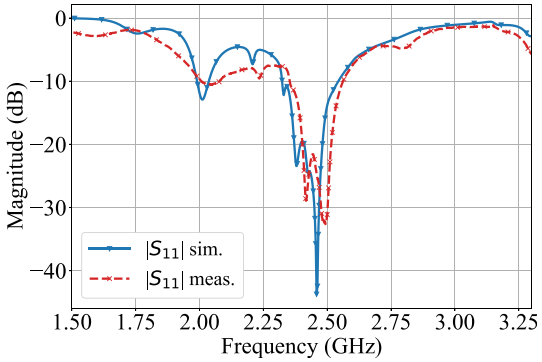

FIGURE 20. Simulated and measured reflection coefficients $|S_{11}|$ for the slot-modified circular CELC metasurface. The measured response validates the predicted wideband behavior.

7.1. Fabricated Prototype

Figure 16 shows the fabricated WR340 cavity, including the conical probe exciter, mounting frame, and alignment holes, to secure interchangeable metasurface plates. The fabricated structure closely matched the geometry used in the simulation, ensuring that the standing-wave magnetic field distribution inside the cavity was reproduced accurately.

7.2. Metasurface Plates and Assembly

Two types of metasurface plates were fabricated: one based on square CELC apertures, and the other based on circular CELC apertures. For each geometry, a second version incorporating lateral-slot perturbations was produced. Figures 17 and 18 show the design drawings and fabricated plates of the slot-modified versions. The alignment holes ensure the repeatable positioning of each plate in the WR340 cavity.

7.3. Measured Reflection Coefficient

Figures 19 and 20 compare the simulated and measured reflection coefficients for the slot-modified square and circular CELC metasurfaces, respectively. In both cases, the measured curves reproduced the main spectral features predicted by the simulation, including the widened matching region introduced by the lateral slot.

The agreement between simulation and measurement is generally good, with small frequency shifts (2–4%) and slight variations in the minimum reflection level attributed to laser-machining edge roughness, tolerances in slot and gap dimensions, finite conductivity and 1.5 mm thickness of the aluminum plates, minor alignment deviations during plate mounting, and residual mismatch in the coaxial-to-waveguide transition of the Anritsu S362E.

7.4. Radiation Pattern Measurement

Far-field radiation patterns were measured in an indoor antenna chamber equipped with RF absorbers to suppress reflections. As shown in Figure 21, the antenna under test (AUT) was mounted on a motorized azimuth rotator (LD Didactic 737405) capable of a full 360° rotation. A log-periodic antenna operating near 2.45 GHz was used as the transmitting antenna, which

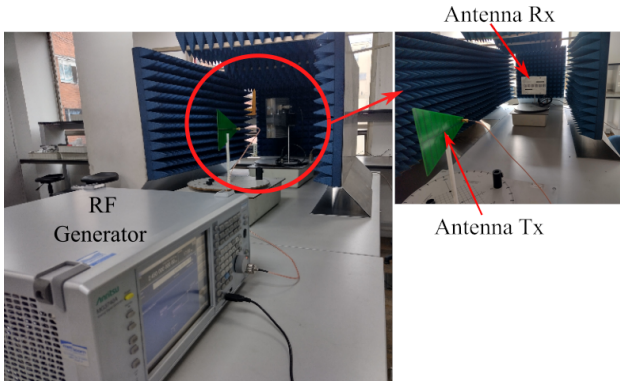

FIGURE 21. Measurement setup for radiation-pattern characterization. The AUT was mounted on a motorized azimuth rotator (LD Didactic 737405) and illuminated by a log-periodic antenna at 2.45 GHz driven by an Anritsu MG3740A RF generator.

was driven by an Anritsu MG3740A RF signal generator. The AUT was connected to the VNA in the receiver mode, enabling the received power to be recorded as a function of the azimuth angle.

Figures 22 and 23 show a comparison between the simulated and measured radiation patterns for the slot-modified square and circular CELC metasurfaces. In both cases, the main lobe appears at the broadside, as expected from the magnetic polarizability weighting. The measured beamwidths and relative sidelobe levels followed the simulated trends, with minor asymmetries attributed to alignment tolerances and residual chamber reflections.

The radiation cuts shown in Figures 22 and 23 correspond to the principal plane of the antenna, which coincides with the conventional E-plane used for the standard antenna characterization. This facilitates a direct comparison between the simulation and measurement under the usual radiation pattern conventions.

The measured resonance frequencies show small shifts with respect to the simulations, within 0.5–1.3% (11–30 MHz around 2.45 GHz), consistent with machining tolerances of ±0.1 mm–0.2 mm. The simulated and measured radiation patterns remained aligned at broadside, with discrepancies mainly limited to sidelobe levels: for the square CELC metasurface

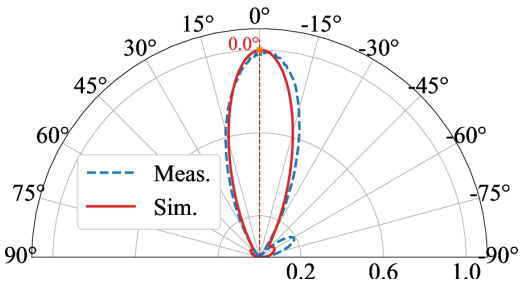

FIGURE 22. Simulated and measured normalized directivity patterns for the slot-modified square CELC metasurface antenna at 2.45 GHz. The main lobe remains at broadside, with small differences observed in the normalized sidelobe levels.

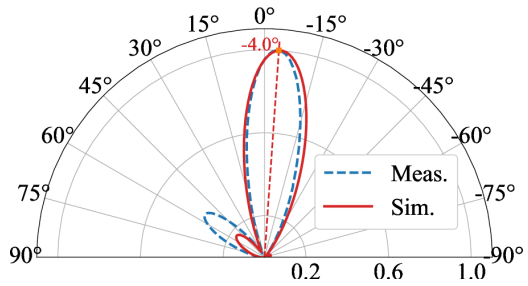

FIGURE 23. Simulated and measured normalized directivity patterns for the slot-modified circular CELC metasurface antenna at 2.45 GHz. The circular geometry yields a smoother normalized radiation distribution and reduced pattern distortion.

TABLE 3. Summary of simulated and measured antenna performances for the slot-modified CELC metasurfaces. Bandwidth is defined at the −10 dB return-loss reference.

Configuration	Gain (dBi)	Realized Gain (dBi)	Simulated Bandwidth (MHz)	Measured Bandwidth (MHz)
Square CELC	8.78	8.83	194	189
Circular CELC	8.25	8.30	222	209

(Figure 22), the normalized sidelobe amplitude increases from 0.082 (simulation) to 0.187 (measurement), while for the circular CELC metasurface (Figure 10), it changes from 0.168 to 0.351. These differences are attributed to fabrication tolerances and minor plate misalignment (up to $\leq$ 0.5 mm), and residual measurement uncertainties.

7.5. Discussion of Experimental Observations

The experimental results supported the main conclusions of this study. The Incremental Difference Method successfully predicted the complex element weights that govern the radiation characteristics of metasurface antennas. Both geometries exhibit improved impedance matching when lateral slots are introduced, and the circular slot configuration provides the broadest operational bandwidth. The measured radiation patterns further validated the metasurface antenna model, demonstrating that the polarizability-based design methodology is effective in practice.

Table 3 summarizes the key performance indicators obtained from the simulation and measurement of slot-modified square and circular CELC metasurface antennas. The results include the simulated and realized gain, as well as the simulated and measured impedance bandwidths defined at the −10 dB reference. The circular slot configuration shows the widest bandwidth in both the simulation and measurement, whereas the square-slot geometry provides a slightly higher gain owing to its more concentrated polarizability distribution.

8. CONCLUSIONS

Beyond validating the metasurface antenna model, the results demonstrated that the Incremental Difference Method can be reliably applied to experimentally designed CELC-based metasurfaces, including bandwidth-enhanced configurations with lateral slots.

This work presented the design, polarizability characterization, and experimental validation of waveguide-fed metasurface antennas based on CELC resonators. Using the Incremental Difference Method, the magnetic polarizability of each unit cell was directly extracted from the perturbed reflection measurements, enabling physically meaningful complex weights for metasurface radiation without additional feed networks.

Square and circular CELC geometries were analyzed under identical WR340 excitations. The circular CELC exhibited a smoother current distribution, lower effective quality factor, and more uniform polarizability profile, yielding weights that are less sensitive to tolerances. The square CELC, although sharper in resonance, provides a slightly higher gain.

The superior uniformity of the circular CELC arises directly from its rotational symmetry, which promotes smoother surface current distributions and reduces the sensitivity to orientation with respect to the local magnetic field. Its lower effective quality factor also produces a gentler Lorentzian phase transition, making the extracted polarizability more tolerant to fabrication errors, and enabling a broader and more stable impedance bandwidth. These properties make the circular geometry particularly attractive for passive metasurface antennas that require moderate bandwidth with robust phase behavior.

Lateral slot perturbations were introduced to overcome the narrowband behavior of Lorentz-type resonators. The simulated and measured $|S_{11}|$ results showed a significant bandwidth improvement, reaching 189 MHz (square) and 209 MHz (circular), which is in close agreement with the simulations. This enhancement was achieved without altering the fundamental resonance mechanism or polarizability based design methodology.

Radiation-pattern measurements further validated the model, with the measured broadside main lobe, beamwidth, and sidelobe levels closely matching the full-wave predictions.

Overall, the combination of magnetic-polarizability mapping and geometry-tailored perturbations provides a compact, passive, and experimentally verified approach for designing bandwidth-enhanced metasurface antennas. Future extensions may include multilayer implementations, polarization-agile elements, and tunable architectures. Despite the bandwidth improvement introduced by the slots, the passive CELC inclusions remain constrained by their Lorentzian dispersion, which limits the full phase control compared with active metasurfaces.

ACKNOWLEDGEMENT

This work was partly supported by Dirección de gestión de recursos para CTel — equipos salud (Convocatoria 844-2019 Ministerio de Ciencia, Tecnología e Innovación, Colombia), project code 130884467291.

REFERENCES

[1] Engheta, N. and R. W. Ziolkowski, *Metamaterials: Physics and Engineering Explorations*, John Wiley & Sons, 2006.

[2] Caloz, C. and T. Itoh, *Electromagnetic Metamaterials: Transmission Line Theory and Microwave Applications*, John Wiley & Sons, 2005.

[3] Shamim, S., A. S. M. Mohsin, M. M. Rahman, and M. B. H. Bhuian, "Recent advances in the metamaterial and metasurface-based biosensor in the gigahertz, terahertz, and optical frequency domains," *Heliyon*, Vol. 10, No. 13, e33272, 2024.

[4] Yang, W., J. Li, D. Chen, Y. Cao, Q. Xue, and W. Che, "Advanced metasurface-based antennas: A review," *IEEE Open Journal of Antennas and Propagation*, Vol. 6, No. 1, 6–24, 2025.

[5] Lin, F. H. and Z. N. Chen, "Low-profile wideband metasurface antennas using characteristic mode analysis," *IEEE Transactions on Antennas and Propagation*, Vol. 65, No. 4, 1706–1713, 2017.

[6] Huang, C., A. Zappone, G. C. Alexandropoulos, M. Debbah, and C. Yuen, "Reconfigurable intelligent surfaces for energy efficiency in wireless communication," *IEEE Transactions on Wireless Communications*, Vol. 18, No. 8, 4157–4170, 2019.

[7] Jian, M., G. C. Alexandropoulos, E. Basar, C. Huang, R. Liu, Y. Liu, and C. Yuen, "Reconfigurable intelligent surfaces for wireless communications: Overview of hardware designs, channel models, and estimation techniques," *Intelligent and Converged Networks*, Vol. 3, No. 1, 1–32, 2022.

[8] Selvaraj, M., R. Vijay, R. Anbazhagan, and A. Rengarajan, "Reconfigurable metasurface: Enabling tunable reflection in 6G wireless communications," *Sensors*, Vol. 23, No. 22, 9166, 2023.

[9] Ashraf, N., T. Saeed, H. Taghvaee, S. Abadal, V. Vassiliou, C. Liaskos, A. Pitsillides, and M. Lestas, "Intelligent beam steering for wireless communication using programmable metasurfaces," *IEEE Transactions on Intelligent Transportation Systems*, Vol. 24, No. 5, 4848–4861, 2023.

[10] Wang, X., J. Q. Han, G. X. Li, D. X. Xia, M. Y. Chang, X. J. Ma, H. Xue, P. Xu, R. J. Li, K. Y. Zhang, H. X. Liu, L. Li, and T. J. Cui, "High-performance cost efficient simultaneous wireless information and power transfers deploying jointly modulated amplifying programmable metasurface," *Nature Communications*, Vol. 14, No. 1, 6002, 2023.

[11] Hu, J., G. Q. Luo, and Z.-C. Hao, "A wideband quad-polarization reconfigurable metasurface antenna," *IEEE Access*, Vol. 6, 6130–6137, 2017.

[12] Lin, M., X. Huang, B. Deng, J. Zhang, D. Guan, D. Yu, and Y. Qin, "A high-efficiency reconfigurable element for dynamic metasurface antenna," *IEEE Access*, Vol. 8, 87 446–87 455, 2020.

[13] Sleasman, T., M. F. Imani, W. Xu, J. Hunt, T. Driscoll, M. S. Reynolds, and D. R. Smith, "Waveguide-fed tunable metamaterial element for dynamic apertures," *IEEE Antennas and Wireless Propagation Letters*, Vol. 15, 606–609, 2016.

[14] Smith, D. R., O. Yurduseven, L. P. Mancera, P. Bowen, and N. B. Kundtz, "Analysis of a waveguide-fed metasurface antenna," *Physical Review Applied*, Vol. 8, No. 5, 054048, Nov. 2017.

[15] Bowen, P. T., A. Baron, and D. R. Smith, "Effective-medium description of a metasurface composed of a periodic array of nanoantennas coupled to a metallic film," *Physical Review A*, Vol. 95, No. 3, 033822, Mar. 2017.

[16] Boyarsky, M., M. F. Imani, and D. R. Smith, "Grating lobe suppression in metasurface antenna arrays with a waveguide feed layer," *Optics Express*, Vol. 28, No. 16, 23 991–24 004, 2020.

[17] Pendry, J. B., A. J. Holden, D. J. Robbins, and W. J. Stewart, "Magnetism from conductors and enhanced nonlinear phenomena," *IEEE Transactions on Microwave Theory and Techniques*, Vol. 47, No. 11, 2075–2084, 1999.

[18] Baena, J. D., R. Marqués, F. Medina, and J. Martel, "Artificial magnetic metamaterial design by using spiral resonators," *Physical Review B*, Vol. 69, No. 1, 014402, Jan. 2004.

[19] Baena, J. D., J. Bonache, F. Martin, R. M. Sillero, F. Falcone, T. Lopetegi, M. A. G. Laso, and J. Garcia-Garcia, "Equivalent-circuit models for split-ring resonators and complementary split-ring resonators coupled to planar transmission lines," *IEEE Transactions on Microwave Theory and Techniques*, Vol. 53, No. 4, 1451–1461, 2005.

[20] Tretyakov, S., *Analytical Modeling in Applied Electromagnetics*, Artech House, 2003.

[21] Schurig, D., J. J. Mock, and D. R. Smith, "Electric-field-coupled resonators for negative permittivity metamaterials," *Applied Physics Letters*, Vol. 88, No. 4, 041109, 2006.

[22] Hand, T. H., J. Gollub, S. Sajuyigbe, D. R. Smith, and S. A. Cummer, "Characterization of complementary electric field coupled resonant surfaces," *Applied Physics Letters*, Vol. 93, No. 21, 212504, 2008.

[23] Sakyi, P., J. Dugan, D. Kundu, T. J. Smy, and S. Gupta, "Waveguide-floquet mapping using surface susceptibilities for passive and active metasurface unit cell characterization," *IEEE Transactions on Antennas and Propagation*, Vol. 72, No. 9, 7110–7121, 2024.

[24] Diaz, I., C. A. S. Fajardo, J. D. B. Doello, and H. Guarnizo, "Subwavelength resonator for the design of a waveguide-fed metasurface antenna," *Progress In Electromagnetics Research C*, Vol. 156, 113–120, 2025.

[25] Yoo, I., M. F. Imani, T. Sleasman, and D. R. Smith, "Efficient complementary metamaterial element for waveguide-fed metasurface antennas," *Optics Express*, Vol. 24, No. 25, 28 686–28 692, Dec. 2016.